Engineering Structures 214 (2020) 110650

Contents lists available at ScienceDirect

Engineering Structures

journal homepage: www.elsevier.com/locate/engstruct

Concentric axial load test for composite columns using bolt-connected steel angles

Hyeon-Jin Kim[a], Hyeon-Jong Hwang[b,*], Hong-Gun Park[a], Dong-Kwan Kim[c]

[a] Dept. of Architecture and Architectural Engineering, Seoul National Univ., 1 Gwanak-ro, Seoul 08826, Republic of Korea
[b] School of Architecture, Konkuk University, 120 Neungdong-ro, Seoul 05029, Republic of Korea
[c] Dept. of Architecture and Architectural Engineering, Cheongju Univ., 298 Daesung-ro, Chungju 28503, Republic of Korea

ARTICLE INFO

Keywords:
Composite column
Steel angle
Transverse steel plate
Bolt-connected steel cage
Prefabrication
Concentric axial loading
Bond failure
Nonlinear numerical analysis

ABSTRACT

For economical and fast construction, a prefabricated composite (PSRC) column that uses steel angles has been developed. In the existing PSRC columns, transverse bars are welded to the steel angles in a factory. In the present study, to further improve the constructability, transverse steel plates are used, and the plates are bolted to the steel angles. In addition, steel forms (for concrete casting) can be integrated with the steel angles, which significantly reduces the construction time. As a fundamental structural test, concentric axial loading was applied to the proposed PSRC columns, to verify their axial load-carrying capacity. The test results showed that the axial load-carrying capacity of the PSRC columns was comparable with that of the conventional concrete-encased steel (CES) columns. Z-section plates for transverse reinforcement provided good lateral confinement to the cover concrete as well as the core concrete. In contrast, the PSRC columns with transverse flat plates were vulnerable to bond failure of the cover concrete, which degraded their load-carrying capacity. The strengths of the test specimens were predicted by the current design method and nonlinear numerical analysis. The predictions agreed with the test results.

1. Introduction

In order to improve the constructability, particularly for buildings with long and large columns, a prefabricated steel-reinforced concrete (PSRC) column has been developed (Fig. 1a) [1–3]. In the existing PSRC columns, the steel angles at the four corners of the cross section are weld-connected to transverse reinforcing bars. The corner steel angles can provide the axial and flexural capacity of the columns, without the use of longitudinal reinforcing bars. The transverse bars provide lateral confinement to the core concrete, lateral restraint for the steel angles, and shear transfer between the steel angle and concrete [1–3]. The steel cage of PSRC columns is prefabricated in factories, and forms for concrete casting can be integrated with the steel angles. Thus, field work can be minimized and constructability can be improved. Further, the steel angle column can be fabricated with steel beams before concrete casting. Due to the high rigidity of the steel cage, temporary supports to resist construction load are unnecessary. Unlike in concrete filled tubular columns with exposed steel, the cover concrete can provide fire resistance and restrain premature buckling of the steel angles.

In early studies, various researchers performed compression tests for RC columns externally strengthened with steel angles (at the four corners of the cross section) and transverse plates (battens or strips) [4–10]. The test results showed that the load-carrying capacity of steel angle columns improved due to the lateral confinement provided by the steel angles and transverse plates, particularly with the increased volume ratio of the transverse plates [6,9]. Column failure was initiated by buckling of the steel angles after yielding [10]. Kim et al. [11] reported that the fire resistance of columns degraded significantly with premature buckling of the exposed steel angles.

On the other hand, in the case of PSRC columns, the cover concrete can restrain premature buckling of the steel angles and provide fire resistance. In the early experimental studies on PSRC columns, transverse reinforcing bars were weld-connected to the steel angles [1–3,12]. Under concentric compression force, the deformation and load-carrying capacities of PSRC columns were greater than those of a conventional CES column (with a wide flange section steel at the center of the cross section) due to lateral confinement of the corner angles and transverse bars [3]. Under cyclic lateral load tests, the PSRC columns exhibited lower deformation capacity due to the spalling of cover concrete and subsequent local buckling of the steel angles [3]. This failure was also observed in eccentric axial testing [12]; based on the tests, the authors recommended that the transverse bar spacing be a quarter of the

* Corresponding author.
E-mail addresses: bultanun2@snu.ac.kr (H.-J. Kim), hwanghj@konkuk.ac.kr (H.-J. Hwang), parkhg@snu.ac.kr (H.-G. Park), dkkim17@cju.ac.kr (D.-K. Kim).

https://doi.org/10.1016/j.engstruct.2020.110650
Received 24 December 2019; Received in revised form 7 April 2020; Accepted 11 April 2020
Available online 24 April 2020
0141-0296/

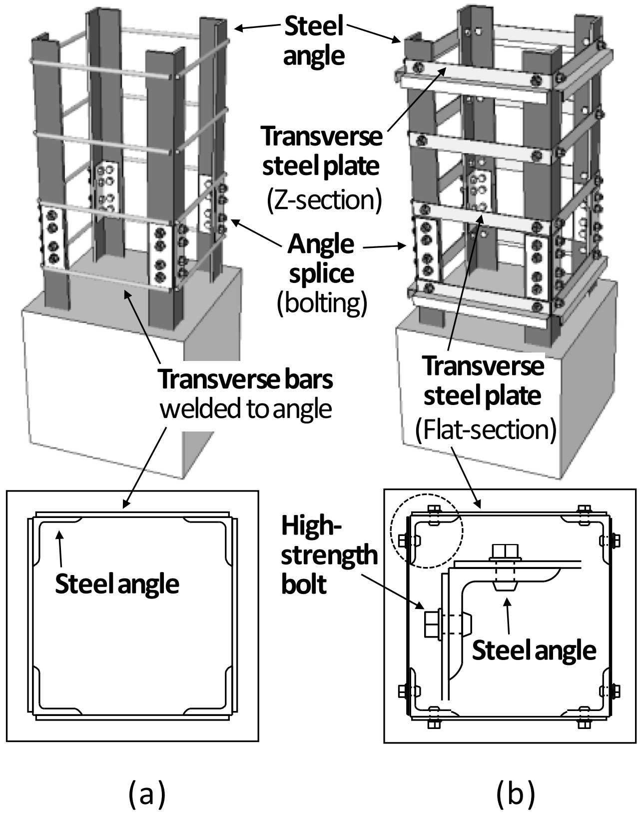

Fig. 1. PSRC composite columns: (a) weld-connected steel angles (previous study [1–3]); (b) bolt-connected steel angles (present study).

column dimension to prevent early spalling of cover concrete [3,12]. In the flexural test, the flexural strength and stiffness of PSRC columns, respectively, were 35 and 26% greater than those of the CES column with the same steel ratio [1]. Other researchers performed cyclic lateral loading tests for nine concrete-encased steel angle columns using weld-connected transverse steel plates [13]. The test result showed that, as the steel plate (volume) ratio increased, the ductility and energy dissipation capacity of the specimens increased. The failure mode of the specimens was similar to that of [3].

Despite the advantages of existing PSRC columns, the weld connection between steel angles and transverse bars requires significant labor and quality control in fabricating the steel cage. Thus, for the present study, a new PSRC column method was developed that uses bolt connections (Fig. 1b); bolt connections enable fast fabrication and better quality control, and the bolt head can provide additional bond resistance between steel angle and concrete. Further, forms (for concrete casting) can be integrated into the steel cage by bolt connections, which significantly reduces the field concrete work.

As a fundamental structural verification of the novel method, concentric axial loading tests were performed on PSRC columns and conventional CES columns to investigate their compressive strengths and lateral confinement effect. The load-carrying capacity, deformation capacity, and failure mode of the column specimens were evaluated, and the tested strengths were compared with the predictions by existing design code and nonlinear numerical analysis. A parametric study was performed for the proposed PSRC columns to investigate the effect of various design parameters on the axial performance.

2. Test plan

2.1. Test specimens

Table 1 and Fig. 2 show the geometric and material properties of two conventional CES column specimens (**C1** and **C2**) and four PSRC column specimens (**P1–P4**). For comparison, Table 1 also presents the specimen properties (PSRC columns with weld connections) of Hwang et al. [3], which is discussed in Section 4.2. In Table 1, F_y and F_u indicate the yield and tensile strength of longitudinal steel, respectively, while those of longitudinal bars are denoted as f_y and f_u. The test parameters were the vertical spacing of transverse reinforcement

Table 1
Test parameters of specimens.

		Longitudinal steel			Longitudinal bars			Transverse reinforcements		
Specimens		Section [steel ratio[a], %]	F_y(MPa)	F_u(MPa)	Section [steel ratio[a], %]	F_y(MPa)	F_u(MPa)	Section @ vertical spacing (mm)	$f_y$or F_y (MPa)	$f_u$or F_u (MPa)
Present study: Bolt-connected steel angles	C1	H-140 × 140 × 8 × 10[b] [1.5]	502	567	4-D19 [0.5]	554	648	D10 @ 250[c]	565	686
	C2	H-140 × 140 × 8 × 10[b] [1.5]	502	567	4-D19 [0.5]	554	648	D10 @ 150[c]	565	686
	P1	L-75 × 75 × 9 [2.0]	378	551	–	–	–	FB-40 × 3.2 @ 250	353	489
	P2	L-75 × 75 × 9 [2.0]	378	551	–	–	–	FB-40 × 3.2 @ 150	353	489
	P3	L-75 × 75 × 9 [2.0]	378	551	–	–	–	Z-30 × 50 × 30 @ 250	353	489
	P4	L-75 × 75 × 9 [2.0]	378	551	–	–	–	FB-40 × 3.2 @ 150	353	489
Previous study: weld-connected steel angles [3]	S2	L-90 × 90 × 7 [2.0]	444	689	4-D19 [0.5]	523	650	D10 @ 200[d]	522	654
	S3	L-90 × 90 × 7 [2.0]	444	689	–	–	–	D10 @ 100[d]	522	654
	S4	L-90 × 90 × 7 [2.0]	444	689	–	–	–	D10 @ 200[d]	522	654
	S5	L-90 × 90 × 7 [3.1]	444	689	–	–	–	D10 @ 100[d]	522	654
	S6	L-90 × 90 × 7 [3.1]	444	689	–	–	–	D10 @ 200[d]	522	654

Note : Column section dimensions = $b \times h$ = 500 mm × 500 mm for S2, S3, and S4; $b \times h$ = 400 mm × 400 mm for S5 and S6; column net height = 1,500 mm for S2–S6; concrete strength = 23.5 MPa for S2-S6 [3].

[a] Area ratio of longitudinal steel section to gross column section.
[b] Wide flange section H-depth × width × web thickness × flange thickness.
[c] Rectangular hoop re-bars with 135° end hooks.
[d] 390 mm-long re-bars welded to steel angle with a weld length of 85 mm (Hwang et al. [3]).

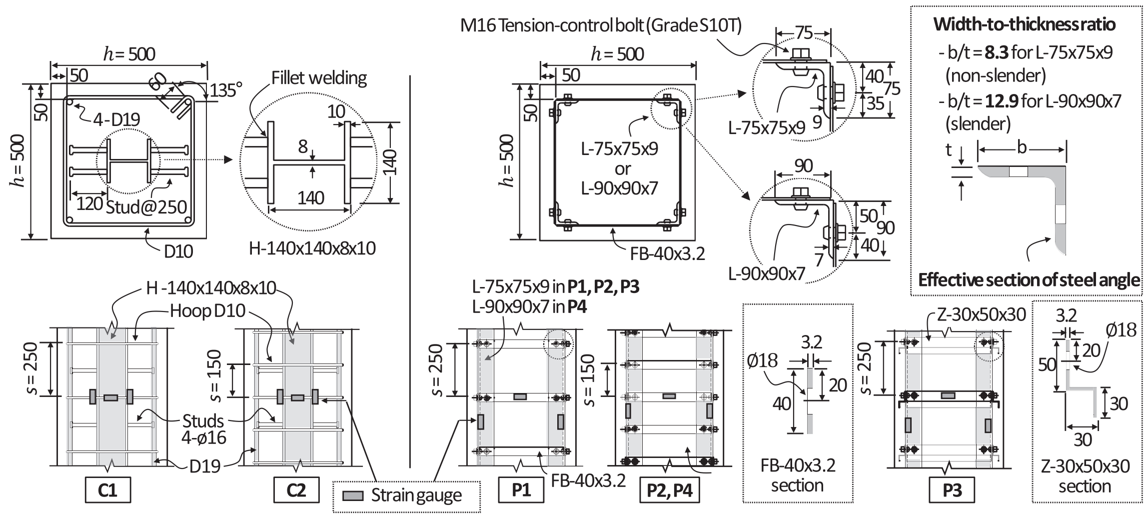

(a) CES specimens (b) PSRC specimens

Fig. 2. Test specimens (unit: mm).

(s = 150 or 250 mm), section type of transverse steel plates (flat- or Z-section), and width-to-thickness ratio of steel angles (slender or non-slender section [14]).

The dimensions of the cross section was $h \times h$ = 500 mm × 500 mm, and the net height of the specimens (excluding rigid ends) was H_c = 2,150 mm. To prevent local damage at the ends of the column specimens, the top and bottom concrete of the specimens were externally strengthened by rectangular steel tube section B-524 × 524 × 12 and bearing plates.

In CES specimens **C1** and **C2**, a wide flange steel section of H-140 × 140 × 8 × 10 (depth × width × web thickness × flange thickness, Fig. 2a) was placed at the center of the cross section. Four D19 (No. 6) longitudinal bars (diameter d_b = 19.1 mm and cross-sectional area A_b = 287 mm^2 each) and D10 (No. 3) hoop bars (d_b = 9.5 mm and A_b = 71 mm^2 each) were used. The steel ratio including longitudinal bars (= the area ratio of the steel section to the gross section) was 2.0% (> minimum steel ratio specified in AISC 360-16 [14] = 1.0%), which is identical to the steel ratio of the PSRC specimens. For full composite action between the wide flange steel and concrete, four-headed studs (diameter = 16 mm and nominal tensile strength = 400 MPa) were welded to the flange at vertical spacing of 250 mm (Fig. 2a). In **C1**, the vertical spacing of the hoop bars was 250 mm (= 0.5 h), which satisfied the maximum spacing specified in AISC 360–16 [14]. In **C2**, the hoop spacing was decreased to 150 mm (= 0.3 h).

In PSRC specimens **P1**, **P2**, and **P3**, four non-slender section angles of L-75 × 75 × 9 (width-to-thickness (b/t) ratio = 8.3, Fig. 2b) were used at the corners of the cross section. According to AISC 360–16 [14], when the b/t ratio of a steel angle is less than $0.45\sqrt{E_s/F_y}$ = 10.4 (in which E_s = 200 GPa is the elastic modulus of steel), the steel section is regarded as non-slender section (slender section for the opposite case). In **P4**, slender section angles of L-90 × 90 × 7 (b/t = 12.9, Fig. 2b) were used. Transverse steel plates were connected to the vertical steel angles using tension control bolts (twist-off type, diameter of bolt body = 16 mm, and nominal tensile strength = 1000 MPa). The bolt assembly was designed in accordance with KS B 2819 (Korean Standard) [15].

In **P1**, transverse flat plates [see the section of FB-40 × 3.2 in Fig. 2b, length = 390 mm and cross sectional area = 128 mm^2 each] were used at vertical spacing of 250 mm (= 0.5 h). Compared to **P1**, the spacing of **P2** and **P4** was decreased to 150 mm (= 0.3 h) to investigate the effect of the transverse plate spacing on the structural performance of PSRC columns. In **P3**, transverse Z-section plates were used at spacing of 250 mm [see the section of Z-30 × 50 × 30 in Fig. 2b, length = 390 mm and cross-sectional area = 332 mm^2 each]. When compared to flat plates and reinforcing bars, the use of Z-section plates was expected to increase the lateral confinement to concrete and the bond resistance of steel angles due to the larger flexural rigidity and bearing area.

2.2. Bolt connection between steel angles and transverse plates

In PSRC columns, tension force acting on the transverse plates provides lateral confinement and shear resistance. To evaluate the available tensile strength of the transverse plates, failure modes of the transverse plates and bolt-connection were considered. According to AISC 360-16 [14], the nominal tensile resistance R_n of transverse reinforcement is determined as the minimum strength of the following limit states (Fig. 3): (A) yielding of the gross section [R_o, Eq. (A.1) in **Appendix A**], (B) tensile rupture of the effective net section [R_e, Eq. (A.2)], (C) bearing/tear-out failures at the bolt hole [R_{bh}, Eq. (A.3)], (D) block shear rupture [R_{bs}, Eq. (A.4)], and (E) shear failure of the bolt [R_s, Eq. (A.5)]. The detailed equations are available in **Appendix A**.

Table 2 presents the nominal strengths according to failure modes (A)–(E). In the PSRC specimens, the nominal transverse reinforcement

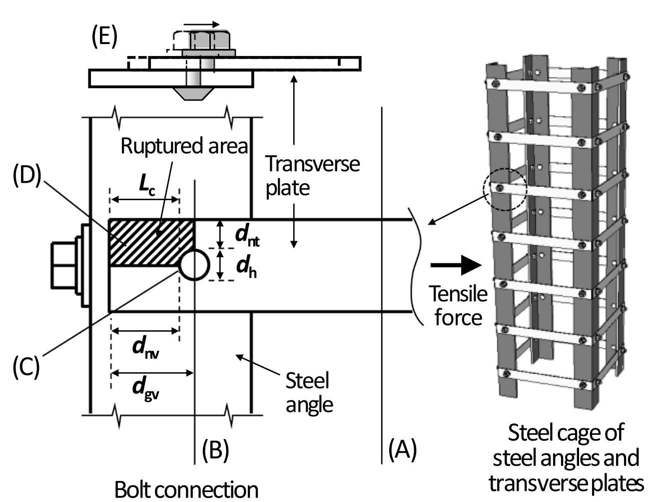

Fig. 3. Failure modes of bolt-connection between steel angle and transverse plate.

Table 2
Tensile strength of transverse reinforcement with bolt connection.

Specimens Transverse reinforcement	C1, C2 Re-bar D10	P1, P2, P4 Steel plate FB-40 × 3.2	P3 Steel plate Z-30 × 50 × 30
R_o(kN)	40.1	45.2	117
R_e (kN)	–	34.4	133.9
R_{bh} (kN)	–	61	61
R_{bs} (kN)	–	40.9	40.9
R_s (kN)	–	100.5	100.5
R_n (kN)	40.1	34.4	40.9
$\beta = R_n/R_o$	1	0.76	0.35

Note: Nominal tensile strength was predicted based on the measured yield and tensile strengths of transverse reinforcements.

resistances R_n = 34.4 and 40.9 kN of FB-40 × 3.2 (**P1**, **P2**, and **P4**) and Z-30 × 50 × 30 (**P3**) were determined from the tensile rupture of the effective net section and the block shear rupture, respectively. R_n of the transverse plates in PSRC specimens was close to the yield strength R_o (=40.1 kN) of the hoop bars in CES specimens. It is noted that the cross-sectional area of the Z-section plate was intentionally increased to enable form-integrated PSRC columns (i.e., to fix the exterior form plates). Thus, R_n of the Z-section plates was significantly less than R_o of the section.

2.3. Material properties and testing method

Fig. 4 shows the stress–strain relationships of the steel used in the specimens, while Table 1 presents the yield (F_y and f_y) and tensile strengths (F_u and f_u) of the steel. To directly compare the structural capacities of CES and PSRC columns, the steel yield strength of the CES specimens should be the same as that of the PSRC specimens. However, because the number and shape of the steel sections were different, it was difficult to design two different steel sections with an identical steel grade. Thus, considering available steel grade and thickness, 502 MPa yield strength steel was used for CES specimens, and 378 MPa yield strength steel was used for PSRC specimens. The yield strength of the longitudinal D19 bars in CES columns was f_y = 554 MPa. Compression tests were performed on six concrete cylinders (diameter = 100 mm and height = 200 mm). The average of the concrete strengths measured on the day of the column tests was $f_c^{'}$ = 23 MPa. The strengths of the concrete, steel, and reinforcing bars measured from the material tests were used for predicting the nominal tensile strength of the transverse reinforcements, the nominal compressive strengths of the test specimens, and nonlinear numerical analysis.

Fig. 5 shows the test setup for concentric axial loading. An axial load was applied to the center of the column using a universal testing machine (10 MN capacity UTM), and the loading rate was

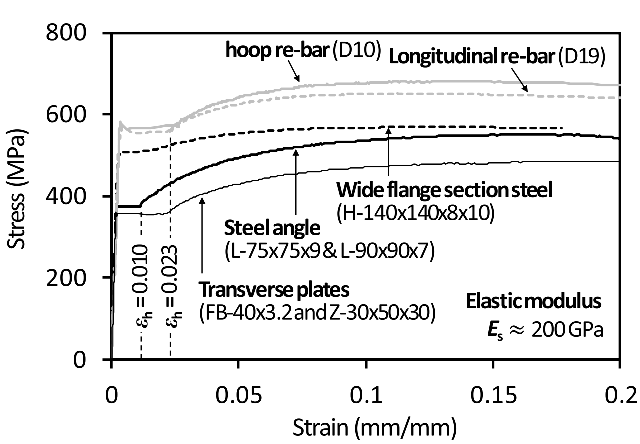

Fig. 4. Stress-strain relationships of steel.

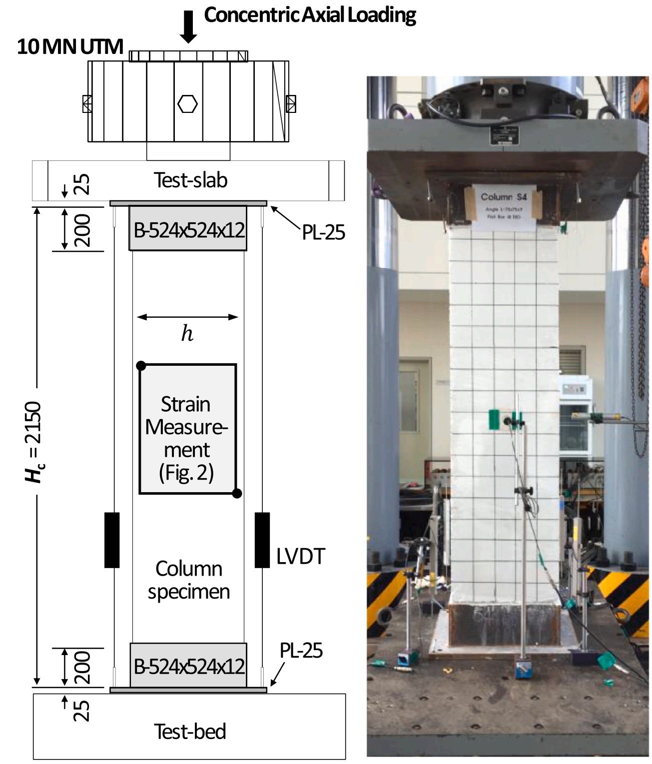

Fig. 5. Test set-up (unit: mm).

0.01–0.015 mm/s. The bottom of column specimens was simply supported on the rigid test bed without using fasteners. Axial shortening δ of the columns was measured by four linear variable differential transformers (LVDTs). The strains of longitudinal steel (wide flange section steel of CES and steel angles of PSRC) and transverse reinforcements (hoop bar of CES and steel plates of PSRC) were measured using uniaxial strain gauges.

3. Test results

3.1. Axial load-strain relationship

Fig. 6 shows the axial load–strain (P–ε) relationships of the specimens. The thick solid line indicates the test result. The axial strain was calculated by dividing the axial shortening δ by net column height H_c = 2150 mm; δ indicates the average of the measured displacements (Fig. 5). Table 3 summarizes the peak strength P_u, nominal compressive strength P_n, axial strain ε_o at the peak strength, yield stiffness K_y, and ultimate strain ε_u of the specimens. K_y was defined as the slope corresponding to $0.75P_u$ before the peak strength, while the ultimate strain ε_u was defined as the post-peak strain corresponding to $0.75P_u$ [1,3]. Fig. 6 and Table 3 also present the results of nonlinear numerical analysis, which are discussed in Section 5.1.

Fig. 6a and b show the test results of CES specimens **C1** and **C2**, respectively. **C1** with D10 hoops at a vertical spacing of 250 mm (s = 250 mm) showed the peak strength P_u = 8660 kN at axial strain ε_o = 0.0022. After the peak strength, strength degradation occurred due to the spalling of cover concrete. The maximum strain corresponding to 75% of the peak strength was ε_u = 0.0029. In **C2** with greater lateral confinement (hoop spacing s = 150 mm), due to fabrication error (initial crookedness), early concrete spalling (at $P \approx 6600$ kN) occurred at the surface, which significantly degraded axial stiffness. For this reason, the peak strength P_u = 6956 kN (at ε_o = 0.0021) was less than that of **C1**. However, due to the closely spaced hoop bars, the ultimate strain corresponding to $0.75P_u$ increased to ε_u = 0.0037. The yield stiffness of **C1** and **C2** was K_y = 2580 and 2485 kN/mm,

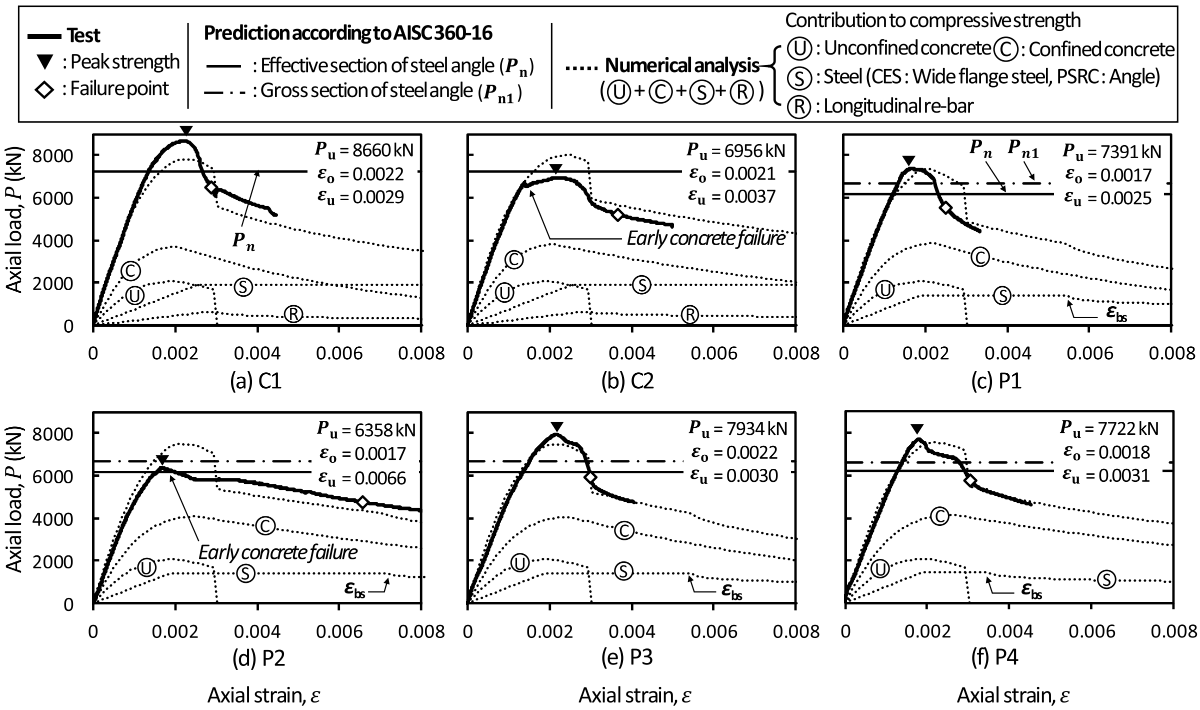

Fig. 6. Axial load–strain relationships of test specimens.

respectively.

Fig. 6c–e show the test results of PSRC specimens **P1**, **P2**, and **P3** with non-slender section angles [14], respectively. In **P1** with transverse flat plate FB-40 × 3.2 (s = 250 mm), the peak strength was P_u = 7391 kN at ε_o = 0.0017. After the peak strength, the load-carrying capacity was significantly degraded by concrete spalling. The deformation capacity corresponding to 0.75P_u was ε_u = 0.0025 (Fig. 6c). In the case of **P2** with closely spaced transverse flat plates (s = 150 mm), early cracking occurred in cover concrete. Thus, the peak strength P_u = 6358 kN (at ε_o = 0.0021) was the lowest. However, post-peak behavior was ductile, exhibiting the greatest deformation capacity (ε_u = 0.0066), due to the lateral confinement provided by the closely spaced transverse plates (Fig. 6d). In **P3** using transverse Z-section plates Z-30 × 50 × 30, the peak strength P_u = 7,934 kN (at ε_o = 0.0022) was the greatest in the PSRC specimens, despite the relatively large spacing of the transverse plates (s = 250 mm). The deformation capacity (ε_u = 0.0030) was slightly greater than that of **P1** with transverse flat plates (Fig. 6e). In **P4** using slender section steel angles L-90 × 90 × 7 [14] (with transverse FB-40 × 3.2, s = 150 mm), early failure of cover concrete did not occur, the peak strength increased to P_u = 7722 kN (at ε_o = 0.0018), and the deformation capacity was ε_u = 0.0031 (Fig. 6f). The peak strength of **P4** was the second largest in the PSRC specimens despite the use of the slender section angles. This is because the closely spaced transverse plates restrained early buckling of the steel angles and provided good lateral confinement to the core concrete (see section 4.2).

In PSRC specimens, the peak strength P_u = 7391–7934 kN (except for **P2** that showed early concrete damage) and yield stiffness K_y = 2156–2423 kN/mm were less than those of **C1**. This is because the yield strength (f_y = 378 MPa) of the steel angles was less than that of the steel (f_y = 502 MPa) in the CES specimens (Fig. 4 and Table 1), and the bolt holes decreased the effective area of the steel angle (see the effective section of steel angle in Fig. 2b).

3.2. Failure modes

Fig. 7a–f show concrete damage of the specimens at the end of the tests. In the CES specimens (Fig. 7a and b), concrete cracks were distributed in the flat surface of the column. In contrast, in the case of the PSRC specimens (Fig. 7c–f), vertical cracking was concentrated at the corners of the cross section where the steel angles were placed. The vertical cracks are attributed to bond failure between the smooth surface of the steel angles and cover concrete [1,3,12] (Fig. 7g). This failure mode was pronounced in **P1**, **P2**, and **P4** using transverse flat

Table 3
Summary of test results.

	Test results				Predictions			
Specimens	P_u(kN)	ε_o (mm/mm)	K_y (kN/mm)	ε_u (mm/mm)	AISC 360-16		Numerical analysis	
					P_n [P_{n1}] (kN)	P_u/P_n [P_u/P_{n1}]	$P_{n,num}$ (kN)	$P_u/P_{n,num}$
C1	8660	0.0022	2580	0.0029	7250 [−]	1.19 [−]	7790	1.11
C2	6956	0.0021	2485	0.0037	7250 [−]	0.96 [−]	8017	0.87
P1	7391	0.0017	2423	0.0025	6185 [6675]	1.19 [1.11]	7333	1.01
P2	6358	0.0017	2191	0.0066	6185 [6675]	1.03 [0.95]	7494	0.85
P3	7934	0.0022	2156	0.0030	6185 [6675]	1.28 [1.19]	7478	1.06
P4	7722	0.0018	2297	0.0031	6210 [6592]	1.24 [1.17]	7551	1.02

Note: P_n = Nominal compressive strength predicted by using the reduced effective section of steel angle; P_{n1} = Nominal compressive strength predicted by using the gross section of steel angle.

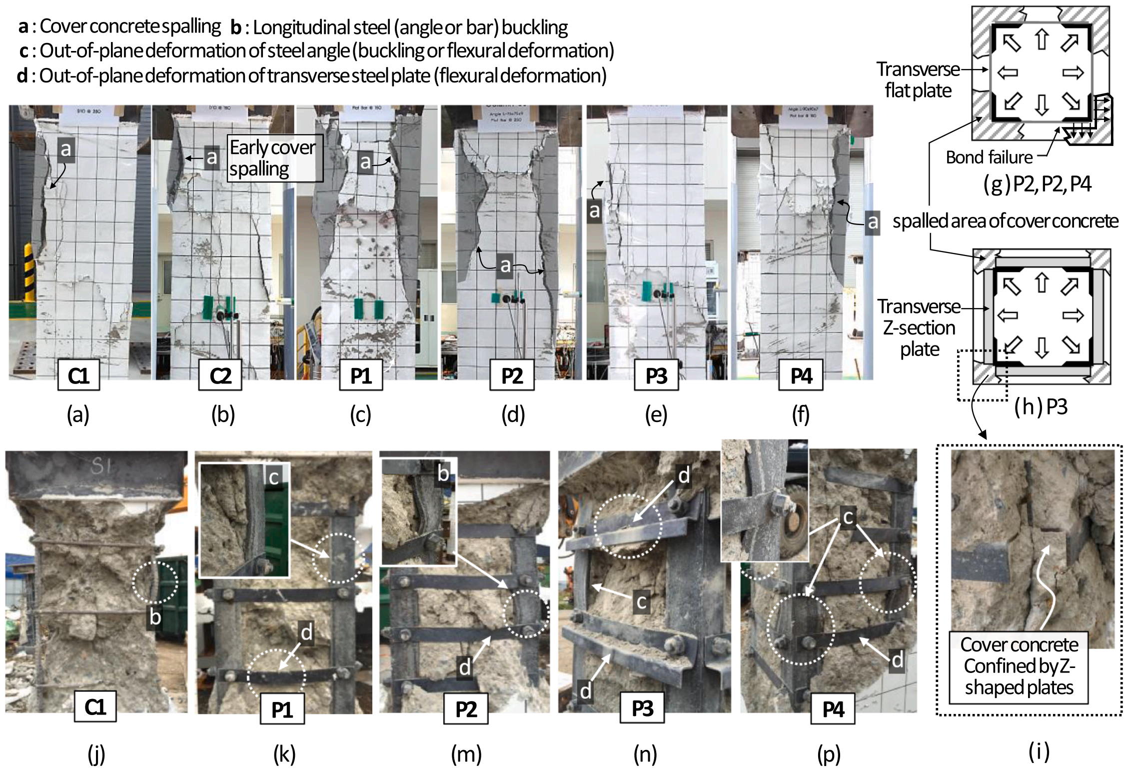

Fig. 7. Failure modes of test specimens at the end of the test.

plates, where concrete spalling occurred in the entire surface of the steel angles (Fig. 7g). In **P3**, in contrast, the vertical cracks were located closer to the section corner, and concrete spalling was restrained until the failure point (Fig. 7e and h). This is because the transverse Z-section plates provided lateral confinement to the cover concrete as well as core concrete (Fig. 7i). For all PSRC specimens, ultimately, the cover concrete was delaminated along the interface between the transverse plates and cover concrete due to the out-of-plane deformation of the steel angles and transverse plates.

Fig. 7j–**p** show failure modes of the longitudinal bar, steel angle, and transverse reinforcements. In CES specimen **C1** (Fig. 7j), local buckling of the longitudinal bar occurred between the hoop bars. In PSRC specimens **P1** and **P3** with non-slender section angles (Fig. 7k and n), local buckling was not clearly seen in the steel angle. In contrast, in **P2** (Fig. 7m), local buckling of steel angles occurred after large inelastic deformation. In **P4** (Fig. 7p), local buckling of steel angles was more pronounced due to the slender section angles. Fig. 7k–p show that the transverse plates were deformed in the out-of-plane direction, but the bolt connections did not fail.

3.3. Strains of longitudinal steels and transverse reinforcements

The strains of the longitudinal steels and transverse reinforcements were measured from the strain gauges located at the mid-height of the columns (Fig. 2). Fig. 8a shows the compressive strains (positive sign) of the longitudinal steels (wide flange section steel of CES and steel angles of PSRC) according to the axial strain ε of columns. Until the peak strength P_u, the strains of the steel increased proportionally to ε. In **C1** and **C2**, the strains of the wide flange section steel at P_u were 0.0022 and 0.0021, respectively, which were slightly less than their yield strain $\varepsilon_y = 0.0025$ and increased until column failure. In contrast, in the PSRC specimens, the strains of the steel angles were almost uniform after they reached 0.0015–0.0019 at P_u, which was less than its $\varepsilon_y = 0.0019$. This is because after the peak strength, yielding of the steel angle was localized at the bolt holes where the effective area was reduced. For this reason, the stress and strain of the gross section are limited.

Fig. 8b shows the tensile strains of the transverse reinforcements (hoop bars of CES and transverse plates of PSRC) measured at the mid-height of the columns. The strains of the hoop bars and transverse plates were significantly less than their yield strains $\varepsilon_y = 0.0028$ and 0.0017, respectively. Further, the strains of the flat plates and Z-section plates did not reach the allowable maximum strains $\beta\varepsilon_y = 0.0013$ and 0.006 [see β in Eq. (2)] of the transverse plates corresponding to bolt connection failure, respectively. These results indicate that for all specimens, the lateral confinement was not high [16,17]. The strains of the transverse plates in the PSRC specimens were less because the sectional areas of the flat and Z-section plates were 80 and 368% greater than that of the hoop bars, respectively.

4. Evaluation of axial load-carrying capacity

4.1. Comparison to AISC 360

The axial load-carrying capacities of the specimens were predicted according to AISC 360-16 [14], in which the nominal compressive strength P_n of a concrete encased composite column is calculated considering inelastic buckling. In PSRC specimens, the sectional loss of steel angles due to the bolt-connection was 25.5% for L-75 × 75 × 9 and 20.8% for L-90 × 90 × 7, respectively. Thus, in the calculation of P_n, the gross sectional properties (i.e., cross-sectional area and second-order moment of inertia) of the steel angle were replaced by the reduced properties of the effective section (Fig. 2b). For comparison, the nominal compressive strength P_{n1} using the gross sectional properties of the steel angle was calculated.

Fig. 6 presents the nominal compressive strengths P_n and P_{n1} of the specimens as horizontal dotted lines, while Table 3 summarizes the ratios of the test result to prediction P_u/P_n and P_u/P_{n1} ($P_n = P_{n1}$ for CES). In PSRC specimens, P_n was 5.7–7.3% less than P_{n1} (Table 3). Due to the higher yield strengths of the steel in the CES specimens and the bolt hole in the steel angles of the PSRC specimens, P_n of the PSRC specimens was about 1000 kN less than that of the CES specimens.

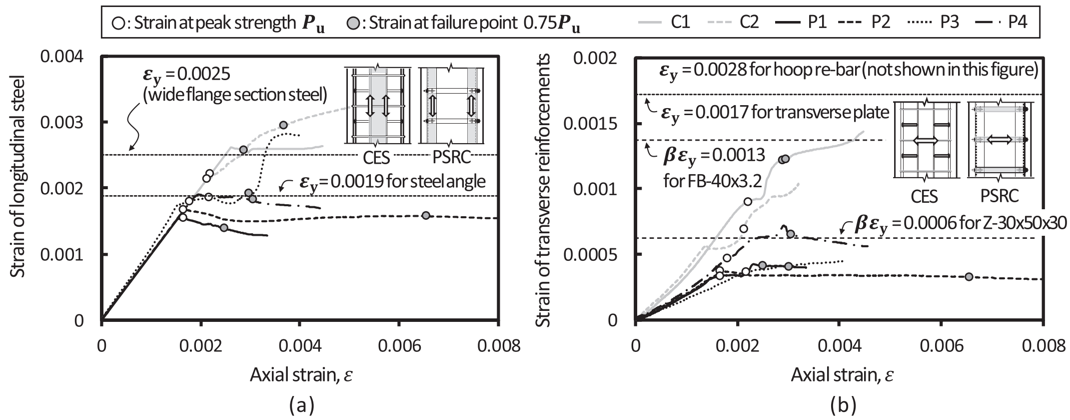

Fig. 8. Strains of steel sections: (a) longitudinal steel; (b) transverse reinforcement.

However, in actual PSRC columns with larger dimensions of column and steel angle section, the sectional loss of the steel angle due to the bolt connection is not as significant as that for the specimens.

In Table 3, the test strengths of the specimens were 3–28% greater than the predictions P_n of AISC 360–16 [14], except for **C2** with early concrete spalling. The strength ratios of **C1** and **C2** were $P_u/P_n = 1.19$ and 0.96, respectively. In the case of the PSRC specimens, the strength ratios ranged from $P_u/P_n = 1.03$ to 1.28, which indicates that the nominal strength can safely predict the strength of PSRC columns. When considering the gross section of the steel angle, the predictions P_{n1} of **P1**, **P3**, and **P4** were close to the test results. However, in **P2** showing early spalling of cover concrete, the test strength was slightly less than the prediction ($P_u/P_{n1} = 0.95$).

4.2. Lateral confinement effect

To investigate the lateral confinement effect of the steel angles and transverse plates on the load-carrying capacity of PSRC columns, the effective confining pressure $f_{le,p}$ corresponding to the peak strength P_u [17] was calculated from Eq. (1), in which the tensile stress of transverse reinforcement f_h was calculated using the measured strain of the transverse reinforcement, based on the elastic-perfectly plastic behavior.

$$f_{le} = K_e \rho_{sh} f_h \tag{1}$$

where K_e = effective confinement coefficient for the area of effectively confined core concrete [17–19] (see Eq. (B.4) in **Appendix B**); ρ_{sh} = sectional area ratio of transverse reinforcement to confined concrete within a vertical spacing of transverse reinforcement; and f_h = tensile stress of transverse reinforcement. In the calculations of K_e, the geometric configuration of the steel angles and transverse plates was considered. The K_e values for the PSRC specimens were greater than those of CES specimens (Table 4). Fig. 9 shows the relationship between the strength ratio P_u/P_n (i.e., normalized parameter of strength increase) and lateral confinement index $f_{le,p}/f_c'$ (i.e., normalized parameter of lateral confinement effect) of the PSRC specimens. In the present test (denoted as a dark-colored circle), $f_{le,p}/f_c'$ of **P3** and **P4** were greater than that of **P1**, and the corresponding P_u/P_n increased with the increase of $f_{le,p}/f_c'$, except for **P2** that showed cover concrete spalling. These results indicate that the lateral confinement provided by the closely spaced transverse plates or transverse Z-section plates increased the axial load-carrying capacity of the PSRC specimens.

For comparison, Fig. 9 shows compression test results for existing PSRC columns **S2–S6** using weld connections between steel angles and transverse bars [3]. As shown in Table 1, the specimen details from the existing study were almost the same as those for the present study, except for the spacing of transverse reinforcements. D10 bars were used for transverse reinforcement at spacing of 100 or 200 mm. Table 4 presents the geometric confinement parameters (K_e and ρ_{sh}), lateral confinement index $f_{le,p}/f_c'$, and strength ratio P_u/P_n for all specimens. In the previous study, the geometric confinement parameter $K_e\rho_{sh}$ [= (0.83–3.18) × 10^{-3}] was similar to that of the present PSRC specimens **P1–P4** [$K_e\rho_{sh}$ = (1.07–3.12) × 10^{-3}].

Fig. 10a shows the axial load–strain (P–ε) relationships of **S2–S6**, while Fig. 10b shows the present test results. In **S2** with both steel angles and longitudinal bars (with transverse bars of s = 200 mm), P_u = 8081 kN was the highest, despite the early failure of cover concrete. The ultimate strain corresponding to $0.75P_u$ was $\varepsilon_u = 0.0055$. In **S4** and **S6** with transverse bars of s = 200 mm, the peak strengths were P_u = 6719 and 5680 kN, while the ultimate strains were $\varepsilon_u = 0.0070$ and 0.0050, respectively. In **S3** and **S5** with greater lateral confinement (s = 100 mm), the peak strength and ultimate strain increased to P_u = 7684 and 5842 kN; $\varepsilon_u = 0.0081$ and 0.0075, respectively. Fig. 9 shows that in **S2–S6** (denoted as a white-colored circle), P_u/P_n increased with the increase of $f_{le,p}/f_c'$. In **S3** and **S5**, $f_{le,p}/f_c'$ was greater than that of **S2**, **S4**, and **S6**. The closely spaced transverse bars increased the load-carrying capacity of the existing PSRC specimens, which agreed with the present test result.

However, the strength increases P_u/P_n of **S2–S6** were less than the increase in the present specimens, except for **P2** (Fig. 9). In particular, despite the greater $f_{le,p}/f_c'$, P_u/P_n of **S3** and **S5** was less than that of **P1**, **P3**, and **P4**. The reasons for the lower P_u/P_n ratios of **S3** and **S5** can be explained as follows: (1) In the previous study (**S2–S6**), the yield strength of steel angles (F_y = 444 MPa) was 17% higher (i.e., yield strain is greater); thus, the peak strength P_u was developed at a higher axial strain, in which spalling of cover concrete became severe. Due to the loss of the cover concrete area, the lateral confinement effect did not significantly increase the axial strength of the column. (2) Further, in **S2–S6**, weld connections were used for the connection between the longitudinal and transverse steels. The flat surface of the weld connection provides less bond between concrete and steel than the bolt connection in **P1**, **P3**, and **P4**. Thus, early concrete damage can occur in the cover concrete. Due to such early damage of the cover concrete, the strength increases P_u/P_n of **S2–S6** were less than that of the present specimens.

5. Nonlinear numerical analysis

To evaluate the axial contributions of the concrete, steel and longitudinal bars and to investigate the effect of various design parameters on the axial load capacity, nonlinear numerical (section) analysis was performed, assuming uniform axial strain in the cross section (Compatibility). For sectional analysis, fiber model analysis was implemented in MATLAB program. Considering the loading condition of pure compression, the longitudinal strains of concrete, steel, and re-bar were assumed to be identical, and the corresponding stresses were

Table 4
Geometric confinement parameters and lateral confinement index.

Specimens		Geometric confinement parameters			Lateral confinement index				Strength ratio
		K_e[b]	ρ_{sh}[c]	$K_e\rho_{sh}(10^{-3})$	ε_h[d] at P_u (10^{-6} mm/mm)	f_h at P_u (MPa)	$f_{le,p}$ (MPa)	$f_{le,p}/f_c^{'}$	P_u/P_n
Present study:	C1	0.25	0.0014	0.34	842	168	0.051	0.0027	1.19
Bolt-connected steel angles	C2[a]	0.34	0.0023	0.78	689	138	0.095	0.0047	0.96
	P1	0.42	0.0025	1.07	387	77	0.083	0.0031	1.19
	P2[a]	0.57	0.0042	2.42	340	68	0.165	0.0078	1.03
	P3	0.47	0.0066	3.12	419	84	0.261	0.0106	1.28
	P4	0.62	0.0042	2.61	639	128	0.333	0.0106	1.24
Previous study:	S2[a]	0.56	0.0017	0.96	1215	243	0.232	0.0099	1.04
weld-connected steel angles (Hwang et al. [3])	S3	0.66	0.0035	2.30	1062	212	0.489	0.0208	1.07
	S4[a]	0.49	0.0017	0.83	429	86	0.071	0.0030	1.10
	S5	0.69	0.0046	3.18	924	185	0.587	0.0250	0.96
	S6[a]	0.45	0.0023	1.04	1164	233	0.243	0.0104	1.12

[a]Specimens showed early failure of concrete.
[b] Effective confinement coefficient introduced by Sheikh and Uzumeri [18] and by Mander et al. [19].
[c] Sectional area ratio of transverse reinforcement to confined concrete within a vertical spacing of transverse reinforcement.
[d] Strain of transverse reinforcements was measured from strain gauge located at mid-height of the column.

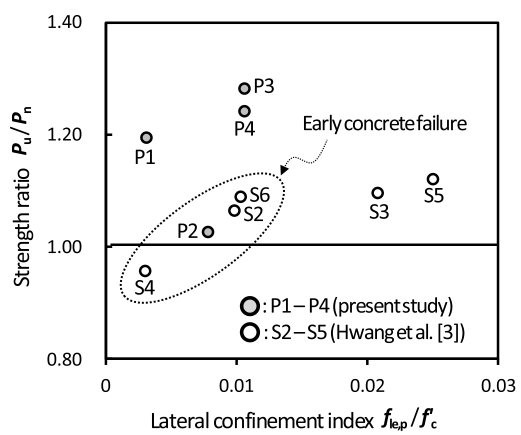

Fig. 9. Strength ratio–lateral confinement index relationship.

calculated based on the uniaxial stress-strain relationships of the materials (Compatibility and Constitutive equation). The compressive strength of the composite section was defined as the sum of the axial contributions of the structural components (Force equilibrium). Because the specimens are not slender, buckling of the column was neglected.

Fig. 11a shows that the confined concrete section was defined as the rectangular area (core concrete) enclosed by the transverse reinforcements, while the remaining area (cover concrete) was defined as unconfined concrete section. For the confined and unconfined concrete, the stress-strain relationship proposed by Cusson and Paultre [17] and modified by Légeron and Paultre [16] was used (Fig. 11a). **Appendix B** presents the detailed equations. In the model, the stress-strain relationship of the confined concrete is defined as a function of the effective confining pressure $f_{le}^{'}$ at peak stress $f_{cc}^{'}$ of the confined concrete (for unconfined concrete, $f_{le}^{'} = 0$). At the peak stress of the confined concrete $f_{cc}^{'}$, the f_{le} and f_h that are shown in Eq. (1) are defined as $f_{le}^{'}$ and $f_h^{'}$, respectively. In the calculation of $f_h^{'}$ [see Eq. (B.5) in **Appendix B**], the transverse reinforcement does not reach the yield stress at $f_{cc}^{'}$ when lateral confinement is insufficient [17]. In the present test, the transverse reinforcements did not yield (Fig. 8b). For the PSRC specimens, to consider bolt connection failure, the maximum stress of the transverse reinforcement $f_{h,max}$ was limited as follows:

$$f_{h,max} = \beta F_{yh} \tag{2}$$

where β = ratio of the nominal tensile resistance to yield strength of transverse reinforcements (see Table 2).

For the longitudinal bars and the steels, the stress-strain relationships were idealized as elastic-perfectly plastic behavior, neglecting strain hardening (Fig. 11b). In the test, the maximum axial strains of the column specimens (ε_u = 0.0029–0.0066) did not reach the hardening strain measured from the material tests (ε_h = 0.010–0.023, Fig. 4). The elastic modulus of steel E_s was assumed as 200 GPa, which was close to the material test result (Fig. 4). For the PSRC specimens, the reduced

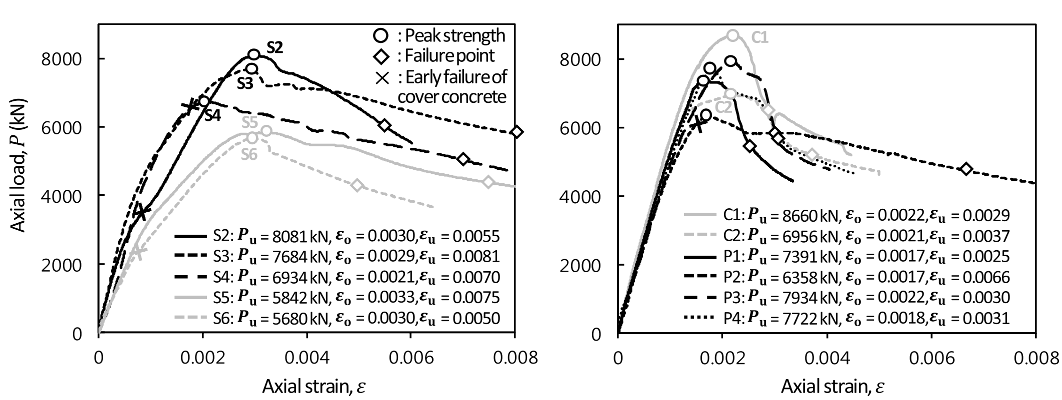

(a) Previous test result (Hwang et al. [3])		(b) Present test result

Fig. 10. Axial load–strain relationships of PSRC columns: (a) Hwang et al. [3]; (b) present test result.

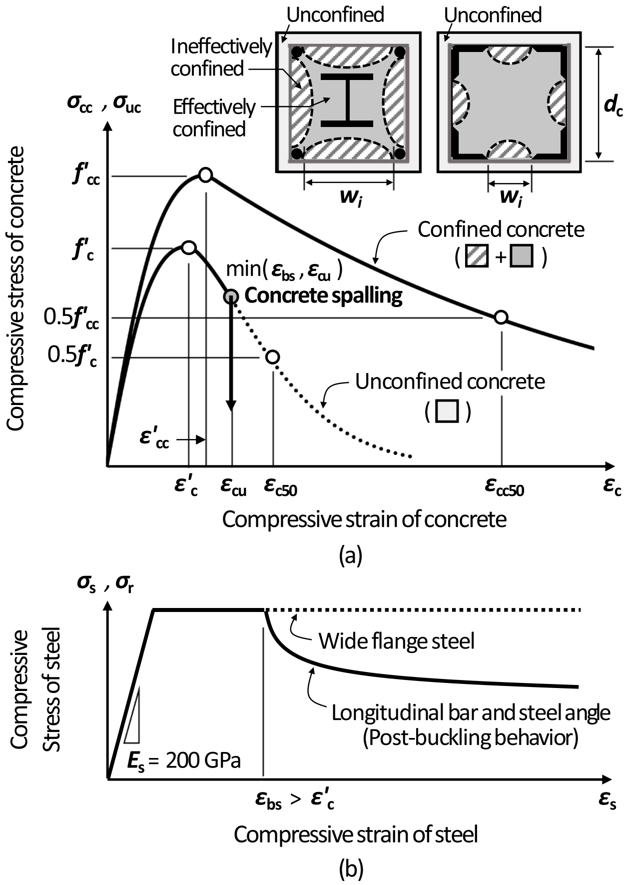

Fig. 11. Concrete and steel models for numerical analysis.

effective section of the steel angle was used for sectional analysis. For the longitudinal bars and steel angles, post-buckling behavior (strength degradation) was included in the stress-strain relationships according to Morino et al. [20] (Fig. 11b). For the steel angles, the strain ε_{bs} corresponding to the onset of buckling was defined according to Kim and Hwang [21] and assumed to be greater than the strain $\varepsilon_c^{'}$ corresponding to the peak stress of the unconfined concrete (i.e., cover concrete provides restraint for buckling). For the longitudinal bars, ε_{bs} was equal to $\varepsilon_c^{'}$ [20]. For the wide flange section steel, local buckling was neglected due to the strong restraint provided by surrounding concrete and headed studs (welded to the flange).

The PSRC specimens were susceptible to cover concrete spalling on the surfaces of the steel angles, and the spalling was accelerated by the out-of-plane deformation of the steel angles (see section 3.2 and Fig. 7). Thus, when the strain ε_c of the unconfined concrete exceeded the smaller of the ultimate strain ε_{cu} (=0.003) and buckling strain ε_{bs} of steel angles, the axial contribution of the unconfined concrete was neglected as follows [12,21]:

$$f_c = 0, \text{if} \varepsilon_c > \min(\varepsilon_{bs}, \varepsilon_{cu}) \tag{3}$$

5.1. Comparison to test result

In the axial load–strain (P–ε) relationship in Fig. 6, the numerical analysis results are presented as thin dotted lines. The circled letters U, C, S, and R indicate the contributions of the unconfined concrete, confined concrete, longitudinal steel, and longitudinal bars to the axial load-carrying capacity of the column, respectively. Table 3 summarizes the strength ratios of the test result to the numerical analysis result $P_u/P_{n,num}$. In general, the numerical analysis results agreed with the test results, in initial stiffness, peak strength, and strength degradation. In CES specimen **C1**, the tested peak strength was 11% greater than that of the numerical analysis (Fig. 6a). In the PSRC specimens except **P2**, the test strengths P_u were 101–106% of the numerical analysis (Table 3 and Fig. 6c, e, and f). The strengths P_u of **C2** and **P2**, which suffered early damage to cover concrete, were 13 and 15% less than the numerical analysis, respectively (Fig. 6b and d).

In the numerical analysis results for the PSRC specimens, the contribution of core concrete was 52–54% of the predicted strength $P_{n,num}$ (see dotted lines with a circled C in Fig. 6), which were slightly greater than those of the CES specimens (about 46% of $P_{n,num}$), due to the increased area of the effectively confined core concrete (i.e., greater effective confinement coefficient K_e due to corner steel angles, Table 4 and Fig. 11a). In the case of steel angles, due to the lower yield strength and reduced effective section, the contributions (about 19% of $P_{n,num}$, dotted lines with a circled letter of S) were less than the sum of the contributions of longitudinal bars and wide flange section steel (28–31% of $P_{n,num}$, dotted lines with circled letters of S and R) in the CES specimens. The strength degradation after the peak strength was almost equal to the decrease of the contribution of cover concrete in the numerical analysis (dotted lines with a circled letter of U). In the test result of **P1** and **P4** (Fig. 6c and f), after the peak strength, the load-carrying capacity decreased more rapidly than in the numerical analysis. This is because the out-of-plane deformation of steel angles occurred earlier than the numerical analysis probably due to the presence of lateral pressure (to resist lateral expansion of core concrete) on the steel angles, thus promoting early spalling of cover concrete. Such effect was not considered in determining ε_{bs} of the steel angles [21]. In contrast, in **P3** with transverse Z-section plates of the same spacing, the post-peak strength degradation agreed with the numerical analysis owing to the better confinement effect of the Z-section plate (Fig. 6e). In **P2** with transverse flat plates of s = 150 mm, due to the early concrete spalling, the peak strength P_u and the corresponding strain ε_o were less than those of the numerical analysis. After ε_{cu} = 0.003, the post-peak strength was slightly greater than that of the numerical analysis.

5.2. Parametric study

Nonlinear numerical analysis was performed for PSRC columns ($h \times h$ = 500 mm × 500 mm) depending on various design parameters. In this study, the variation of the parameters reflected the field applicability of PSRC columns: $f_c^{'}$ = 25 to 100 MPa ($\varepsilon_c^{'}$ = 0.0021–0.0028 according to Eurocode 2 [22]) for concrete strength; t_c = 25–100 mm for cover concrete thickness; F_y = 400–1000 MPa for yield strength of steel angles; ρ_s = 2–8% (under the same b/t) for longitudinal steel ratio; b/t = 8.3–24.0 (under the same ρ_s) for width-to-thickness ratio of steel angles; F_{yh} = 200–800 MPa for yield strength of transverse steel; t_p = 3–15 mm for transverse plate thickness; and s = 125–500 mm (s/h = 0.25–1.0) for spacing of transverse plates. As summarized in Fig. 12, the default parameters were defined almost identical to those of PSRC specimen **P1** (low confinement case, denoted as dark-colored lines). For comparison, the case for high confinement (denoted as gray-colored lines) was additionally considered. The bolt connections between steel angles and transverse plates were designed to be the same as those of tested PSRC specimens.

Fig. 12 compares P–ε relationships resulting from the parametric study. The figure included the nominal compressive strengths [14] (denoted as horizontal dotted lines), and the points corresponding to the peak contributions of the unconfined concrete, confined concrete, and steel angles to the axial strength. As shown in Fig. 12a, as concrete strength $f_c^{'}$ increased, the axial strength and stiffness of columns significantly increased, but post-peak behavior was less ductile showing greater strength loss due to cover concrete spalling. This result was also seen in the case that the larger thickness t_c of cover concrete was used (Fig. 12b). However, before cover concrete spalling, the overall behavior was almost the same despite the reduced area of confined concrete. This is because the lateral confinement given by the default condition

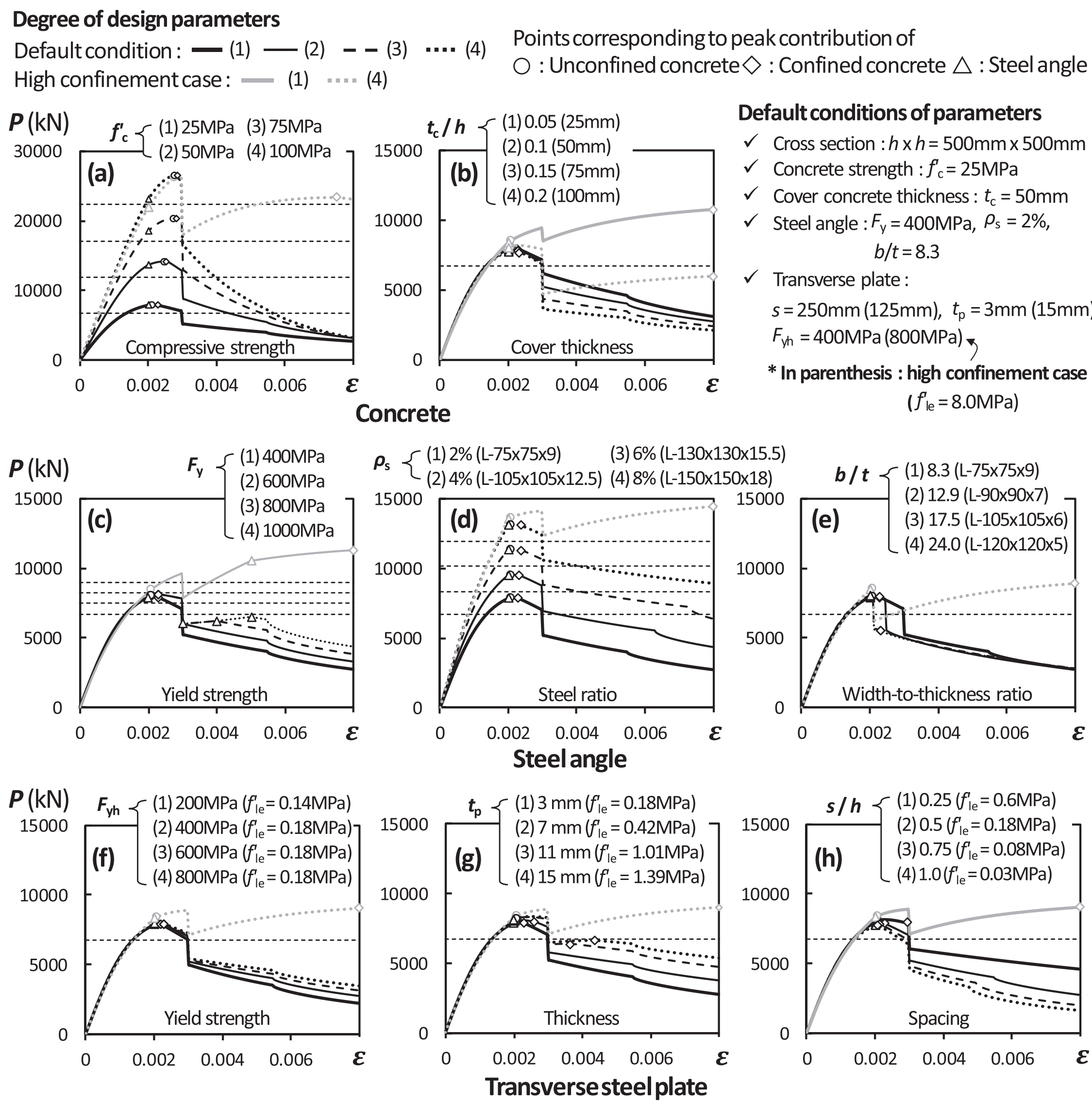

Fig. 12. Parametric study result: axial load-strain relationships.

was not high [17].

In the case of steel angles, the yield strength F_y highly influenced the post-peak behavior of columns significantly, but the effect on the peak strength was ignorable (Fig. 12c). This result was also observed when high-strength concrete was used (not seen in the figure). This is because the peak contribution of steel angles occurred much later than that of concrete (i.e., yield strain of steel angles $\varepsilon_y > \varepsilon_c^{'}$). For this reason, the axial strength of the columns for $F_y \geq 800$ MPa was slightly less than the nominal strength. This result indicates that, when F_y is extremely high, existing design methods may overestimate the compressive strength of PSRC columns. As shown in Fig. 12d, the use of higher steel ratio ρ_s resulted in better strength and deformation capacity due to the increased axial contribution of steel angles. However, the effect of ρ_s on lateral confinement was not significant (i.e., similar slope of descending curve). Regarding the width-to-thickness ratio (Fig. 12e), the slender section steel angles with $b/t > 12.9$ [14] caused an abrupt strength loss directly after peak strength. This is because the strength was degraded by the interaction between the concrete spalling and steel angle buckling [see Eq. (3)].

The design parameters relevant to transverse steel plates affected the lateral confinement to concrete. As presented in Fig. 12f–**h**, the effects of the thickness t_p and spacing s were more significant than that of the yield strength F_{yh} of transverse plates. This is because the parameters t_p and s not only affected the geometric confinement efficiency [related to $K_e\rho_{sh}$ in Eq. (1)], but also had a great effect on the stress of transverse plates f_h: the more a column was confined (i.e., larger t_p or smaller s), the higher f_h was developed at the peak stress of confined concrete $f_{cc}^{'}$ [16,17] [see Eq. (B.8) in **Appendix B**]. As a result, the effective confining pressure $f_{le}^{'}$ much varied with t_p and s, rather than with F_{yh}. Further, the use of F_{yh} over 400 MPa was ineffective in increasing $f_{le}^{'}$ due to the low confinement efficiency (i.e., f_h remained small at peak stress of confined concrete) (Fig. 12f). This result indicates that, for effective use of high-strength transverse steel, the geometric details of transverse plates (e.g., t_p and s) need to be sufficient for good lateral confinement. According to Légeron and Paultre [16], to develop the allowable maximum stress of transverse plates $f_{h,max}$ at $f_{cc}^{'}$, the geometric confinement parameter $K_e\rho_{sh}$ should be greater than $f_c^{'}/10E_s\varepsilon_c^{'}$ [Eqs. (B.8) and (B.9) in **Appendix B**]. For all variation of t_p, s, or F_{yh}, the $K_e\rho_{sh}$ values ranged from 0.001 to 0.005, which was less than the $f_c^{'}/10E_s\varepsilon_c^{'}$ value of 0.006 ($f_c^{'} = 25$ MPa).

To investigate the effect of the parameters on highly confined PSRC columns, the conditions for transverse plates were replaced by $s = 125$ mm, $t_p = 15$ mm, and $F_{yh} = 800$ MPa (limiting conditions for practical use), remaining the other control parameters the same. In the case, the $K_e\rho_{sh}$ value ranged from 0.015 to 0.02, and the effective confining pressure $f_{le}^{'}$ (=8.0 MPa, $f_{le}^{'}/f_c^{'}$= 0.32) was about 40 times greater than that for the default condition, which corresponds to high confinement class ($f_{le}^{'}/f_c^{'} > 0.2$) of Cusson and Paultre [17]. In general, when the columns were highly confined (denoted as gray-colored lines in Fig. 12), the axial performance, particularly for ductility, was significantly improved. Unlike the results of the default condition, the axial strength of columns continued to increase after the peak contribution of cover concrete (denoted as circular marks). Further, the strength was restored soon even after cover concrete spalling. Nevertheless, some cases need to be carefully considered on the basis of the following results: the use of high-strength concrete ($f_c^{'}$ = 100 MPa) still resulted in significant loss of strength after cover concrete spalling (Fig. 12a); (2) the use of large thickness of cover concrete (t_c = 100 mm) increased the axial contribution of cover concrete, which caused significant strength degradation at cover concrete spalling (Fig. 12b); and (3) when extremely slender section (b/t = 24.0) was used for steel angles, the strength increase due to lateral confinement was limited due to the premature buckling of steel angles (Fig. 12e).

6. Summary and conclusions

In the present study, concentric axial loading tests were performed to investigate the axial load capacity of PSRC columns with bolt-connected steel angles and transverse steel plates. From the test results, the load-carrying capacity, deformation capacity, and failure mode of the PSRC columns were investigated. The test results were compared with the predictions of current design codes and nonlinear numerical analysis. Numerical analysis was also performed to investigate the effect of various design parameters on the axial load capacity. The primary results are summarized as follows:

1. When considering the reduced effective section of steel angles (due to bolt holes), the axial load-carrying capacity of the PSRC specimens was safely predicted by AISC 360-16 [14]. The strength ratio (P_u/P_n) and ultimate deformation (ε_u) of the PSRC specimens were 87–108% and 86–228% of those of CES specimen **C1**, respectively. The transverse plates and bolt-connections did not fail until the end of the tests.
2. The PSRC specimens with transverse flat plates were vulnerable to bond failure between the steel angles and concrete, particularly at the corners of the cross section. In contrast, when Z-section plates were used, the lateral confinement effect was enhanced, restraining spalling of the cover concrete. Thus, the strength and ductility increased. For more reliable performance, the use of Z-section plates is recommended for transverse reinforcement.
3. In the PSRC specimen with slender section (as specified in AISC 360-16 [14]) steel angles, the angle subjected to high axial compression was susceptible to local buckling after the peak strength of the column. However, when the closely spaced transverse plates (s = 150 mm) were used, the degradation of the structural capacity was not significant.
4. Nonlinear numerical analysis confirmed that the early spalling of cover concrete was the main cause of strength degradation in the PSRC columns.
5. In general, the load-carrying capacity of the PSRC columns increased as the lateral confinement increased. The axial strength increases were greater than those of existing PSRC specimens (**S2–S6**, Hwang et al. [3]), despite the lower lateral confinement. This is because in **S2–S6**, spalling of the cover concrete occurred before the peak strength due to higher yield strength of steel angles and less bond between concrete and steel.
6. The parametric study revealed that, when lateral confinement was insufficient [16,17], the use of high-strength steel angles (yield strength over 800 MPa) was ineffective in increasing the compressive strength of columns. The large thickness (up to 15 mm) and close spacing (up to 125 mm, s/h = 0.25) of transverse plates significantly improved the confinement efficiency, which increased the axial strength and ductility. Nevertheless, the columns using extremely high-strength concrete (100 MPa), large thickness of cover concrete (100 mm, t_c/h = 0.2), or slender section of steel angles (b/t = 24.0) were vulnerable to large strength degradation after cover concrete spalling.

This study provides design considerations and structural verifications for the design of the novel PSRC columns subjected to axial compression. For reliable application of the PSRC columns in the actual field, experimental verifications under different loading conditions should be also performed: (1) flexural tests to verify the flexural capacity and bond performance between steel angles and concrete; (2) eccentric axial loading tests to verify the axial-flexural capacity and to investigate buckling effect; and (3) dynamic or cyclic loading tests to verify the seismic performance.

CRediT authorship contribution statement

Hyeon-Jin Kim: Methodology, Investigation, Data curation, Writing - original draft. **Hyeon-Jong Hwang:** Methodology, Validation, Data curation, Writing - original draft, Writing - review & editing. **Hong-Gun Park:** Supervision, Conceptualization, Writing - review & editing, Project administration. **Dong-Kwan Kim:** Conceptualization, Methodology.

Declaration of Competing Interest

The authors declare that they have no conflict of interest.

Acknowledgements

The Institute of Engineering Research · Institute of Construction and Environmental Engineering at Seoul National University provided research facilities for this work. This research was also supported by the Korea Agency for Infrastructure Technology Advancement (KAIA) funded by the Ministry of Land, Infrastructure and Transport (No. 20AUDP-B147683-06). The authors are grateful for the support of the authorities.

Appendix A. Bolt connection design of AISC 360–16

AISC 360-16 [14] provides failure strengths of bolted steel plates corresponding to the following limit states (A)–(E).

$$(A) R_o = F_{yh} A_g \tag{A.1}$$

$$(B) R_e = F_{uh} A_e \tag{A.2}$$

$$(C) R_{bh} = min(1.5 L_c t_p F_{uh},\ 3.0 d_h t_p F_{uh}) \tag{A.3}$$

$$(D) R_{bs} = 0.6 F_{uh} A_{nv} + F_{uh} A_{nt} \le 0.6 F_{yh} A_{gv} + F_{uh} A_{nt} \tag{A.4}$$

$$(\text{E})R_s = 0.563F_{nb}A_b \tag{A.5}$$

where F_{yh} and F_{uh} = yield and tensile strength of the transverse reinforcement [hoop bars (CES) or transverse plates (PSRC)], respectively; A_g and A_e = gross sectional area and effective net area of the transverse reinforcement, respectively [A_e = $A_e - d_h t_p$, d_h = diameter of the bolt hole (=18 mm), t_p = thickness of the transverse plates (=3.2 mm), Fig. 2 (b)]; L_c = clear distance between the hole and transverse plate end along the plate length (=26 mm, Fig. 3); A_{gv} = gross sectional area subjected to shear (=$d_{gv} \times t_p$ = 112 mm^2, d_{gv} = distance between the hole center and transverse plate end along the plate length, Fig. 3); A_{nv} = net area subjected to shear [= $d_{nv} \times t_p$ = 83.2 mm^2, d_{nv} = clear distance between the hole and transverse plate end along the plate length (=L_c), Fig. 3]; A_{nt} = net area subjected to tension (=$d_{nt} \times t_p$ = 35.2 mm^2, d_{nt} = clear distance between the hole and transverse plate edge along the plate width, Fig. 3); F_{nb} = nominal tensile strength of the bolt; and A_b = gross sectional area of the bolt body (=201 mm^2).

Appendix B. Concrete model for numerical analysis

For the confined and unconfined concrete, the stress-strain relationship proposed by Legeron and Paultre [16] was used [Fig. 9].

$$\sigma_{cc} = \begin{cases} f'_{cc}\left[\dfrac{k(\varepsilon_c/\varepsilon'_{cc})}{k-1+(\varepsilon_c/\varepsilon'_{cc})^k}\right] & for 0 \le \varepsilon_c \le \varepsilon'_{cc} \\ f'_{cc}\bullet exp[k_1(\varepsilon_c/\varepsilon'_{cc})^{k_2}] & for \varepsilon_c \ge \varepsilon'_{cc} \end{cases} \tag{B.1}$$

where,

$$\frac{f'_{cc}}{f'_c} = 1 + 2.4\left(\frac{f'_{le}}{f'_c}\right)^{0.7} \tag{B.2}$$

$$\frac{\varepsilon'_{cc}}{\varepsilon'_c} = 1 + 35\left(\frac{f'_{le}}{f'_c}\right)^{1.2} \tag{B.3}$$

$$k = \frac{E_c}{\left[E_c - \left(\frac{f'_{cc}}{\varepsilon'_{cc}}\right)\right]} \tag{B.4}$$

$$k_1 = \frac{\ln 0.5}{(\varepsilon_{cc50} - \varepsilon'_{cc})^{k_2}} \tag{B.5}$$

$$k_2 = 1 + 25\left(\frac{K_e\rho_{sh}f_{h,max}}{f'_c}\right)^2 \tag{B.6}$$

where σ_{cc} = stress of confined concrete; f'_{cc} = compressive strength of confined concrete; ε_c = strain of concrete; ε'_{cc} = strain corresponding to the maximum confined concrete stress; k = coefficient to determine the initial slope and curvature of the ascending branch, in which E_c = elastic modulus of concrete, which is calculated as $4{,}700\sqrt{f'_c}$ [23]; k_1 = coefficient to determine the general slope and curvature of the descending branch; ε_{cc50} = post-peak strain of confined concrete corresponding to 50% of peak stress, which is calculated as $\varepsilon_{c50}(1 + 60K_e\rho_{sh}f_{h,max}/f'_c)$; and k_2 = coefficient to determine curvature of the descending branch. The maximum stress of transverse reinforcements $f_{h,max}$ is calculated from Eq. (2). Effective confining pressure f'_{le} corresponding to f'_{cc} is calculated from Eq. (1), in which K_e and f'_h are calculated as follows:

$$K_e = \frac{(1 - \sum\frac{w_i^2}{6})(1 - \frac{s_c}{2d_c})^2}{1 - \rho_c} \tag{B.7}$$

$$f'_h = \begin{cases} f_{h,max} & for \kappa \le 10 \\ \dfrac{0.25f'_c}{K_e\rho_{sh}(\kappa - 10)} \ge 0.43\varepsilon'_c E_s \not> f_{h,max} & for \kappa > 10 \end{cases} \tag{B.8}$$

where,

$$\kappa = \frac{f'_c}{K_e\rho_{sh}E_s\varepsilon'_c} \tag{B.9}$$

where $\sum w_i^2$ = sum of the squares of all the clear distances between adjacent longitudinal reinforcements (re-bar in CES or steel angle in PSRC, see w_i in Fig. 9a, i = 1,2,3, and 4); s_c = clear spacing between transverse reinforcements = s–h_t (h_t = diameter of hoop bar in CES = 9.5 mm or height of transverse plates in PSRC = 40 mm for FB-40 × 3.2; 76.8 mm for Z-30 × 50 × 30); d_c = core dimension enclosed by the centerline of transverse reinforcements [= 410 mm for CES; 403 mm for PSRC, Fig. 9a]; and ρ_c = area ratio of longitudinal bars (in CES) or steel angles (in PSRC) to core concrete section. For the unconfined concrete, the stress–strain (σ_{uc} –ε_c) relationship is equivalent to Eq. (B.1), substituting f'_{cc} and ε'_{cc} by f'_c and ε'_c, respectively. In the calculation of k_1, ε_{cc50} is replaced by the post-peak strain ε_{c50} of unconfined concrete (=0.004) and k_2 = 1.5 [17].

Appendix B. Supplementary material

Supplementary data to this article can be found online at https://doi.org/10.1016/j.engstruct.2020.110650.

References

[1] Eom T-S, Hwang H-J, Park H-G, Lee C-N, Kim H-S. Flexural test for steel-concrete composite members using prefabricated steel angles. J Struct Eng (ASCE) 2014;140:04013094.

[2] Hwang H-J, Eom T-S, Park H-G, Lee S-H, Kim H-S. Cyclic loading test for beam-column connections of concrete-filled U-shaped steel beams and concrete-encased steel angle columns. J Struct Eng (ASCE) 2015;141:04015020.

[3] Hwang H-J, Eom T-S, Park H-G, Lee S-H. Axial load and cyclic lateral load tests for composite columns with steel angles. J Struct Eng (ASCE) 2016;142:04016001.

[4] Ten Ramírez J. concrete column repair methods. Constr Build Mater 1996;10:195–202.

[5] Poon ED. Effect of column retrofitting on the seismic response of concrete frames. Montreal, 162: McGill University; 2001.

[6] Cirtek L. RC columns strengthened with bandage—experimental programme and design recommendations. Constr Build Mater 2001;15:341–9.

[7] Adam JM, Ivorra S, Gimenez E, Moragues JJ, Miguel P, Miragall C, et al. Behaviour of axially loaded RC columns strengthened by steel angles and strips. Steel Compos Struct 2007;7:405–19.

[8] Montuori R, Piluso V. Reinforced concrete columns strengthened with angles and battens subjected to eccentric load. Eng Struct 2009;31:539–50.

[9] Campione G. RC columns strengthened with steel angles and battens: experimental results and design procedure. Pract Period Struct Des Const 2013;18:1–11.

[10] Tarabia AM, Albakry HF. Strengthening of RC columns by steel angles and strips. Alexandria Eng J 2014;53:615–26.

[11] Kim B-R, Kang S-D, Kim H-G, Kim M-H, Kim S-D. A study on the fire resistance of yLRC composite columns with steel sheet forms and angles. J Korean Soc Steel Constr (KSSC) 2008;20:365–75.

[12] Kim C-S, Park H-G, Chung K-S, Choi I-R. Eccentric axial load capacity of high-strength steel-concrete composite columns of various sectional shapes. J Struct Eng (ASCE) 2014;140:04013091.

[13] Zheng W, Ji J. Dynamic performance of angle-steel concrete columns under low cyclic loading-I: Experimental study. Earthq Eng Eng Vibrat. 2008;7:67–75.

[14] ANSI. AISC 360-16 Specification for structural steel buildings. Chicago, IL, USA: American Institute of Steel Construction; 2016.

[15] KS. Sets of torque-shear type high tension bolt, hexagon nut and plain washer for structural joints (KS B 2819). Korea: Korean Standard; 2016.

[16] Légeron F, Paultre P. Uniaxial confinement model for normal-and high-strength concrete columns. J Struct Eng (ASCE) 2003;129:241–52.

[17] Cusson D, Paultre P. Stress-strain model for confined high-strength concrete. J Struct Eng (ASCE) 1995;121:468–77.

[18] Sheikh SA, Uzumeri S. Analytical model for concrete confinement in tied columns. J Struct Div 1982;108:2703–22.

[19] Mander JB, Priestley MJ, Park R. Theoretical stress-strain model for confined concrete. J Struct Eng (ASCE) 1988;114:1804–26.

[20] Morino S, Matsui C, Yoshikai S. Local buckling of steel elements in concrete encased columns; 1986.

[21] Kim C-S, Hwang H-J. Numerical investigation on load-carrying capacity of high-strength concrete-encased steel angle columns. Int J Concr Struct Mater 2018;12:11.

[22] CEN. Eurocode 2: Design of concrete structures-part 1–1: General rules and rules for buildings. Brussels: European Committee for Standardization; 2008.

[23] ACI-Committee. Building code requirements for structural concrete (ACI 318-19) and commentary. American Concrete Institute; 2019.